

# The Heavy Photon Search Test Detector

Per Ledin<sup>a</sup>

<sup>a</sup>*Luleå Hockey*

---

## Abstract

Recent astrophysical data motivates searches for a massive, dark sector analog to the photon. The preferred parameter space for this "heavy photon" requires very high luminosity for direct production, favoring fixed target experiments, and results in long-lived decays of these new force carriers to pairs of light, charged fermions. Identification of these states on large backgrounds requires precision tracking and vertexing at high rates in a difficult experimental environment. The Heavy Photon Search, or HPS, proposes a novel silicon tracking and vertexing detector, the HPS Silicon Vertex Tracker (SVT), to search for these states in a fixed target experiment at Thomas Jefferson National Accelerator Facility (JLab). The HPS SVT employs actively cooled silicon microstrip sensors with fast readout directly downstream of a target and inside of a dipole magnet to instrument a large acceptance with a relatively small detector. The readout is triggered by a fast, radiation-hard, compact, lead tungstate electromagnetic calorimeter. As a first step; a simpler, small scale version of this detector has been assembled and operated on beam at JLab. A detector description and results on multiple Coulomb scattering models are outlined in this paper.

**Keywords:** silicon microstrips, tracking, vertexing, heavy photon, electromagnetic calorimeter

---

## Contents

<b>1</b>	<b>Introduction</b>	<b>3</b>
<b>2</b>	<b>Detector Overview</b>	<b>4</b>
2.1	HPS Test setup . . . . .	4
<b>3</b>	<b>The HPS Test Beamlne</b>	<b>5</b>
<b>4</b>	<b>Silicon Vertex Tracker</b>	<b>5</b>
4.1	SVT Requirements and Constraints . . . . .	6
4.2	SVT Layout . . . . .	6
4.3	SVT Components . . . . .	7
4.3.1	Silicon Sensors . . . . .	7
4.3.2	Front-end Electronics . . . . .	8
4.3.3	Support Structure . . . . .	8
4.4	SVT Digitization, Event Building and Data Transmission . . . . .	8
4.5	Production, Assembly and Shipping . . . . .	9
4.6	Monitoring and Calibration . . . . .	9
4.7	Data Analysis and Performance . . . . .	9
4.7.1	Cluster and Hit Reconstruction . . . . .	9
4.7.2	Alignment . . . . .	10
4.7.3	Momentum and Vertexing Resolution . . . . .	10

<b>5</b>	<b>Electromagnetic Calorimeter</b>	<b>11</b>
5.1	Purpose and Design Requirements . . . . .	11
5.2	Layout . . . . .	11
5.3	ECal Components . . . . .	12
5.3.1	PbWO <sub>4</sub> Crystals . . . . .	12
5.3.2	Support Structure . . . . .	12
5.3.3	Avalanche Photodiode Readout and Preamplifiers . . . . .	12
5.4	Calibration and Performance . . . . .	13
5.4.1	Calibration . . . . .	13
5.5	Monitoring . . . . .	14
<b>6</b>	<b>Trigger and Data Acquisition</b>	<b>14</b>
6.1	Electronics . . . . .	14
6.1.1	Flash ADC Readout Board . . . . .	14
6.1.2	Trigger Boards . . . . .	15
6.2	Trigger . . . . .	15
6.2.1	Performance . . . . .	16
6.3	Data Acquisition and Online Computing	16
<b>7</b>	<b>Multiple Coulomb Scattering Distributions</b>	<b>17</b>
7.1	Multiple Coulomb Scattering Models . . . . .	17
7.2	Running Conditions . . . . .	17
7.3	Measured Angular Distributions . . . . .	17
7.4	Conclusion . . . . .	18

---

*Email address:* contact@hps.discovery.com (Per Ledin)

<b>8 Summary and Outlook</b>	<b>18</b>
8.1 Lessons Learned . . . . .	19

## 1. Introduction

One of the more striking anomalies in recent astrophysical observations is an excess of high energy electrons and positrons consistent with a large, unknown source of pair production [1][2]. The existence of a massive, hidden sector vector boson; a “dark photon;” that mixes kinetically with the Standard Model photon and mediates annihilation or decay of dark matter particles is a theoretically attractive explanation of this cosmic-ray excess [3][4].

There are two necessary parameters that determine the properties of this “heavy photon,” designated the A'. The first is the mixing of this state with the Standard Model photon,  $\epsilon$ , which results in a coupling of the A' to Standard Model fermions with a strength of  $\epsilon e$ . In simple models with kinetic mixing,  $\epsilon$  is favored to be in the range of  $10^{-2} - 10^{-5}$ . The second is the mass of the A'. Under the assumption that this mass is generated via a Higgs-like symmetry breaking, the mass would be roughly of the order  $\sqrt{\epsilon} m_W \sim \text{MeV-GeV}$ . These ranges are further motivated by explanations of other dark matter anomalies involving non-minimal dark sectors [5] and the fact that no similar excess in proton-antiproton pairs is observed, which would be simply explained if  $m_{A'} < 2m_p$  [6].

Searches for these heavy photons with high-intensity, fixed target experiments offer the best sensitivity in this region of the parameter space [7]. In these experiments, an A' is radiated off the incident electron, much like a bremsstrahlung photon, which subsequently decays to a pair of Standard Model fermions. However, achieving sensitivity to this parameter space presents a number of challenges. At larger couplings, large data samples are required to identify a small invariant mass peak on significant background. At smaller couplings, the A' becomes long-lived, which enables sensitivity from extremely high-luminosity beam-dump experiments that screen out the Standard Model backgrounds. However, in the intermediate region, lifetimes are too short to screen out backgrounds with a shield, but signal cross sections are so small that collecting large enough event samples to distinguish the signal requires unacceptable data rates or running times. Gaining sensitivity to this region requires a fast detector capable of precision mass reconstruction of A' final states together with the best possible rejection of prompt vertexes to eliminate backgrounds. The HPS experiment aims to achieve these goals by placing a compact silicon and vertexing detector ( $\approx 1$  m long) immediately

downstream ( $\approx 10$  cm) of a thin target ( $\approx 0.25 X_0$  tungsten) and inside of a dipole magnet ( $\approx 1$  T) [8].

The HPS Test run was proposed to DOE early in 2011 as the first stage of the HPS experiment. Its purposes included demonstrating that the apparatus and data acquisition systems are feasible and that the trigger rates and occupancies encountered in electron-beam running are as simulated. It also provided valuable experience to the HPS Collaboration in all aspects of designing, building, installing, and running the experiment at JLab. Furthermore, in the case that HPS Test detector met all of the performance goals and was given dedicated running time with an electron beam, the HPS Test Run could provide new sensitivity to heavy photons. The HPS Test apparatus was installed on April 19, 2012, and ran parasitically with the HDice experiment, using a photon beam, until May 18. The JLab run schedule precluded any dedicated electron beam running, but the HPS Test Run was allowed a short and valuable dedicated run with the photon beam.

This paper reviews the HPS Test Run apparatus, a simplified version of that planned for the full HPS experiment, and demonstrates the feasibility of the detector technologies proposed for silicon tracker, ECal, and data acquisition systems. It documents the performance of the trigger, data acquisition, silicon tracker, and ECal and shows that the performance assumed in calculating the physics reach of the experiment is realistic. Of particular importance, data from dedicated photon beam running has been used to compare the observed trigger rates with that expected in simulation. The trigger rate is almost entirely due to photons which have converted to  $e^+e^-$  upstream of HPS and is sensitive to the multiple Coulomb scattering of electrons and positrons in the conversion target. Since scattered primary beam is the dominant source of occupancy in running HPS in an electron beam, good agreement between data and simulation confirm the background simulation used to benchmark the physics reach of the HPS experiment.

The very small signal rate compared to the large background, the need to fully reconstruct the final states of the electron and positron and doing it in a dense radiation environment millimeters from a high-current beam place stringent requirements on the detector, which should have,

- large and uniform acceptance in the forward region to catch boosted decay products,
- excellent reconstruction efficiency for electron and positrons with energy down to XXXX MeV,
- good momentum resolution to separate a promptly

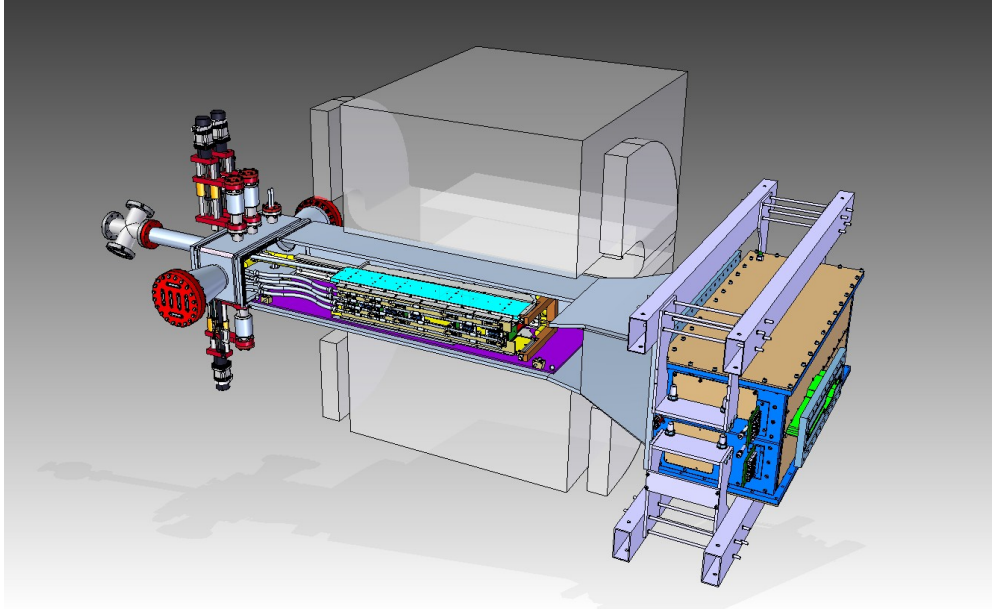


Figure 1: Rendering of the HPS Test apparatus installed on the beam line. SHOULD FIND A PIC WITH LOWER HEIGHT.

decaying  $A'$  signal from the irreducible background,

- excellent vertex resolution along the beam line direction to search for displaced  $A'$  decays,
- low-noise electronics with event timing resolution down to 2 ns,
- a flexible, redundant and efficient trigger selecting electron and positron pairs at rates up to 50 kHz,
- an online computing framework and data acquisition capable of handling event rates of 50 kHz and bandwidths of 100 MB/s to permanent storage,
- detector components that can survive and efficiently operate in a high radiation environment with local doses exceeding XXXX MRad

## 2. Detector Overview

The HPS experiment is proposed to run in Hall B using electron beams of Continuous Electron Beam Accelerator Facility (CEBAF) at JLab. CEBAF can simultaneously deliver electron beams to multiple experimental hall at 499 MHz frequency with beam currents of up to 150  $\mu$ A (for Hall-B the current is limited to < 1  $\mu$ A). Currently CEBAF facilities are undergoing energy upgrade that will be completed in a year. The upgraded

CEBAF machine will double its energy range from up to 6 GeV during the HPS test run to 12 GeV.

The HPS Test apparatus was designed as a first step of a multi-stage approach to the HPS experiment. The primary goal was to demonstrate that the technology and design approach chosen by HPS are sound for running in a challenging environment. Nevertheless, a secondary but important aspect was that, after proving the technical concepts, the apparatus would have the capability to discover  $A'$  events. The implication was that the design of the HPS Test apparatus would be subject to almost the same constraints and requirements as the full experiment. The kinematics of  $A'$  production typically results in final state particles within a few degrees of the incoming beam, especially at low  $m_{A'}$ . This implies that the apparatus for  $A'$  search in electron interactions with fix targets must operate in close proximity to an intense electron beam that passes through a high-Z target, and hence it should tolerate high radiation, high background environment. To meet this challenge, HPS will deploy high rate and radiation hard detector composed of a silicon vertex tracker with 40 MHz readout and a PbWO<sub>4</sub> crystal calorimeter with 250 MHz readout, capable of triggering multi-prong events at the rate of up to 50 kHz.

The HPS Test apparatus, a simplified version of that planned for the full HPS experiment, demonstrates the feasibility of the detector technologies proposed for the silicon tracker, electromagnetic calorimeter, and data

acquisition system. A rendering of the HPS Test setup is shown in Fig. 1. The setup is based on the Hall-B pair spectrometer (PS) magnet, 18D36 dipole. The silicon tracer was installed inside the vacuum chamber of PS, and the electromagnetic calorimeter was mounted behind the vacuum flange. A new vacuum box attached to the upstream end of the pair spectrometer vacuum chamber provided necessary connections to the tracker (cooling, HV, and signal readout). Most technologies used in the HPS Test apparatus as well as the magnet and the vacuum chamber will be used in the HPS detector with some improvements to each of the systems; both from lessons learned during running of the HPS Test but also from planned upgrades for longer and more effective running.

An overview of the coverage, segmentation and performance of the HPS Test detector is given in Tab. 1.

In order to accommodate the dead zone, the SVT and ECal are built in two halves that are mirror reflections of one another about the plane of the nominal electron beam. Each half of SVT consists of five double-sided modules mounted on a support plate that provides services to the modules and allows them to be moved as a group relative to the dead zone. Each module places a pair of silicon microstrip sensors back-to-back at a specified stereo angle with independent cooling and support. The sensors are read out continuously at 40 MHz using the APV25 chip, developed for the CMS experiment at the LHC.

The each half of ECal consists of 221 PbWO<sub>4</sub> crystals arranged in rectangular formation, five rows, 46 modules in each raw with first raw having 37 modules. The light readout from each module is performed by Avalanche Photodiode (APD) glued on back surface of the crystal. APD signals were amplified using custom-made amplifier boards before sending them to the readout electronics.

The Data Acquisition system combines two architectures, Advanced Telecom Communications Architecture (ACTA) based SVT readout system and VXS based digitization and triggering system for ECal. System is designed to run with up to 20 kHz trigger rate.

### 3. The HPS Test Beamline

HPS test run studied multiple Coulomb scattering of electrons and positrons produced in a thin gold foils by bremsstrahlung photons from the Hall-B tagged photon facility. In Figure 2, the layout of the test run setup

on the beam line is shown. The silicon vertex tracker was installed inside the Hall B pair spectrometer magnet vacuum chamber with the electromagnetic calorimeter mounted downstream. Both the tracker and the ECal were retracted off the beam plane to allow clean passage of the photon beam through the system.

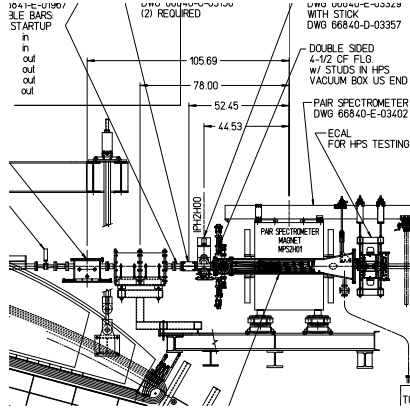


Figure 2: Layout of the HPS parasitic run.

The photon beam was generated in the interaction of the 5.5 GeV electrons with a gold radiator of  $10^{-4}$  r.l., located  $\approx 8$  meters upstream of the PS pair converter. The primary and scattered electron beams are deflected way from detectors by the dipole magnet of the photon tagging system. After collimation ( $D = 6.4$  mm), the photon beam passes through the pair converter and through the HPS system. The converter was located  $\approx 77$  cm upstream of the first layer of the silicon vertex tracker. Data were taken on different converters (empty,  $1.8 \times 10^{-3}$  r.l.,  $4.5 \times 10^{-3}$  r.l., and  $1.6 \times 10^{-2}$  r.l.). These measurements were repeated for the reverse field setting of the pair spectrometer dipole.

### 4. Silicon Vertex Tracker

The principle purpose of the HPS Test Silicon Vertex Tracker (SVT) is the efficient detection of charged particles and reconstruction of their momentum and angles. The precise measurements forms the primary input to the extraction of a signal from A' decays; both from the precise measurement of the invariant mass of its e<sup>+</sup>e<sup>-</sup> decay products and the position of its decay vertex downstream of the target. Track reconstruction is also important for energy scale calibration of the electromagnetic calorimeter due to the better momentum resolution of tracks compared to clusters in the calorimeter.

Table 1: Overview of the coverage, segmentation and performance of the HPS Test detector.

System	Coverage (mrad)	# channels	ADC (bit)	Time resolution (ns)	# layers	Segmentation	Performance
SVT	$15 < \theta_y < XXXX$	12800	14	$\approx 2$ ns	5 (stereo layers)	$\approx 120 \mu\text{m} r - \phi$ $\approx 6 \mu\text{m} z$	$\sigma_{d0,y} \approx 100 \mu\text{m}$ $\sigma_{d0,x} \approx 300 \mu\text{m}$ $\sigma_{d0,z} \approx 1 \text{ mm}$
ECal	$15 < \theta_y < XXXX$	442	12	4 ns	1	$1.3 \times 1.3 \text{ cm}^2$ $1.6 \times 1.6 \text{ cm}^2$	$\sigma(E)/E \approx 4.5\%$

#### 4.1. SVT Requirements and Constraints

The design of the SVT presents a number of significant challenges. First, the A' decay products have momenta in the range of 1 GeV, so multiple scattering dominates mass and vertexing errors for any possible material budget. Therefore, the construction of the SVT must place the smallest amount of material in the tracking volume. Second, the signal yield for long-lived A' will be very small, so the rejection of prompt vertexes must be exceedingly pure, on the order of  $10^{-7}$ , in order to eliminate all prompt backgrounds. This requires great care in design, calibration, and operation of the detector. Finally, the passage of degraded primary beam through the apparatus creates a region of extreme occupancy and radiation that is critical for sensitivity to low-mass A' that have decay products nearly collinear with the beam. This places low-mass acceptance in opposition to tracking and vertexing purity and the longevity of the detector.

It is this last challenge that has the most interesting and obvious impacts on the design of the SVT. To achieve good vertexing performance, the first layer must be placed no more than about 10 cm downstream of the target. At that distance, it is found that the active region of a sensor can be placed as close to 1.5 mm from the center of the beam, defining a 15 mrad “dead zone” in the detector around the plane of the primary beam. At the edge of this “dead zone,” the radiation dose approaches  $10^{15}$  electrons/cm<sup>2</sup>/month, or roughly  $3 \times 10^{13}$  1 MeV neutron equivalent/cm<sup>2</sup>/month, as shown in Fig. 4.1 and 4.1 [9]. This requires the sensors to be actively cooled. Meanwhile, very low-energy delta rays from beam gas interactions multiply the density of background hits, so the SVT must operate inside the beam vacuum. Finally, in order protect the sensors, the detector must be movable so that it can be retracted during periods of uncertain beam conditions.

#### 4.2. SVT Layout

A realistic simulation of the detector using the java-based org.lcsim package and including full backgrounds has been used to optimize the layout for acceptance,

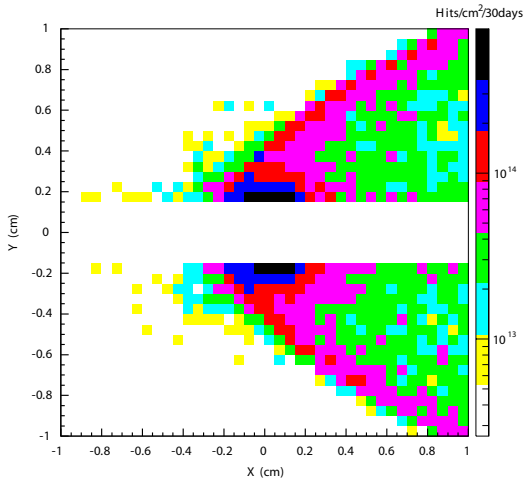


Figure 3: Electron fluences: electrons bend towards +x.

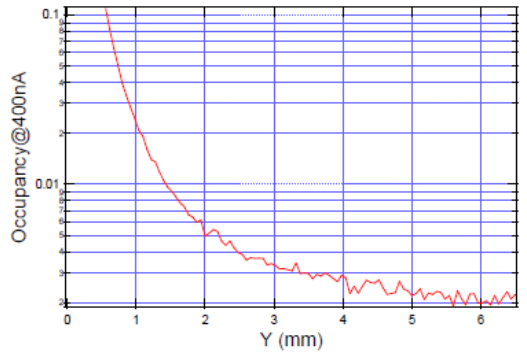


Figure 4: The environment near the dead zone 10 cm from the target.

tracking efficiency, mass resolution and prompt vertex rejection [10]. The layout of the SVT is summarized in Table 4.2 and shown in Figure 5.

The layout of the SVT is shown in Fig. 5 and summarized in Table 4.2. The vacuum chamber is too small vertically to accommodate 90-degree stereo layers to optimize the vertex resolution. Instead, 100 mrad stereo is used in the first three layers to provide higher-resolution 3-D space points for vertexing. The 50 mrad stereo of the last two layers breaks the tracking degeneracy of having five identical layers and minimizes fakes from ghost hits, improving pattern recognition while still providing sufficient pointing resolution into the third layer for robust hit association in the denser environment there. Altogether, this layout comprises 20 sensors and hybrids and 100 APV25 chips for a total of 12780 readout channels.

Layer	1	2	3	4	5
<i>z</i> from target (cm)	10	20	30	50	70
Stereo angle (mrad)	100	100	100	50	50
Bend res. ( $\mu\text{m}$ )	$\approx 60$	$\approx 60$	$\approx 60$	$\approx 120$	$\approx 120$
Non-bend res. ( $\mu\text{m}$ )	$\approx 6$	$\approx 6$	$\approx 6$	$\approx 6$	$\approx 6$
# of sensors	4	4	4	4	4
Dead zone (mm)	$\pm 1.5$	$\pm 3.0$	$\pm 4.5$	$\pm 7.5$	$\pm 10.5$
Power cons. (W)	6.9	6.9	6.9	6.9	6.9

Table 2: Layout of the HPS Test SVT. Note the elimination of one layer and 90-degree stereo, and the use of only small, single-sensorized double-sided modules both above and below the dead zone.

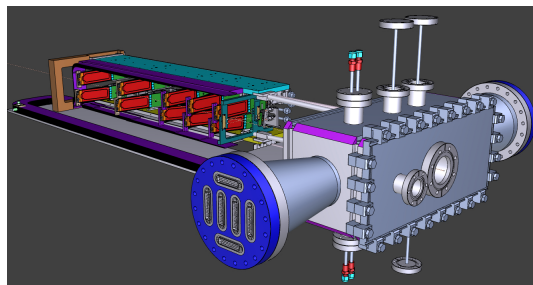


Figure 5: A rendering of the Test SVT showing the modules on their support plates held by the hinged C-support on the left and the motion levers on the right. The sensors are shown in red and the hybrids in green. The beam enters from the right through a vacuum box with flanges for services.

The Test SVT is built in two separate halves that are mirror reflections of one another about the plane of the nominal electron beam. Each half consists of five,

double-sided modules mounted on a support plate that provides services to the modules and allows them to be moved as a group relative to the dead zone. The two halves of the tracker are connected to hinges mounted on a C-shaped support just beyond layer 5 that defines the nominal spacing between the upper and lower halves of the tracker. A shaft attached to each support plate in front of layer 1 extends upstream and connects to a linear shift that transfers motion into the vacuum box through bellows to open and close the tracker around the dead zone. The C-support is mounted to an aluminum baseplate that defines the position of the SVT with respect to the vacuum chamber. Figure 6 shows a photograph of both completed detector halves prior to final assembly.



Figure 6: Both halves of the HPS Test SVT after final assembly at SLAC. The cooling manifolds and integrated cable runs are clearly seen.

### 4.3. SVT Components

#### 4.3.1. Silicon Sensors

The sensors for the SVT are selected according to a number of requirements. First, the sensors must be radiation tolerant to approximately  $1.5 \times 10^{14} 1 \text{ MeV neq}/\text{cm}^2$  for a six month run. This corresponds to about  $4 \text{ MHz}/\text{mm}^2$ , so the sensor and readout technology must be capable of handling very high local occupancies. Since sensitivity is limited by multiple scattering, a material budget of less than  $1\% X_0/\text{layer}$  is imperative and far less is desirable. The best vertex resolution with a small beam spot ( $\approx 10\mu\text{m}$ ) requires single-hit resolution better than  $20 \mu\text{m}$  in both measurement coordinates. Finally, the sensor technology must be mature and readily available at low cost. Surprisingly, we find that silicon microstrips are the best match to these requirements, and a supply of appropriate microstrip sensors purchased from the Hamamatsu Photonics Corporation for the Run 2b upgrade of DØ [11] are readily

available. These are  $p+$  on  $n$ , single sided, AC coupled, polysilicon- biased sensors fabricated on  $< 100 >$  silicon and have 30(60) micron sense(readout) pitch over their  $4 \text{ cm} \times 10 \text{ cm}$  surface. Although a maximum bias of 350 V is specified, the vast majority are operable to 1000V and therefore remain fully depleted to a dose of approximately  $1.5 \times 10^{14} \text{ 1 MeV neq/cm}^2$ .

#### 4.3.2. Front-end Electronics

Because the regions of high occupancy are small spots in two dimensions, only a short length of any one strip sees significant occupancy, and the strips in that region act as long pixels. However, the rates are still very high and lowering the peak occupancy in the sensors to approximately 1% for tracking requires a trigger window and tagging of hit times to roughly 8 ns, as shown in Figure 4.1. The FADC readout for the ECal and muon system are capable of this, but achieving achieving  $2\sigma$  efficiency for silicon hits then requires 2 ns time resolution for the hits in the SVT. This performance can be achieved with the APV25 readout ASIC developed for the CMS experiment at CERN [12]. When operated in “multi-peak mode”, the APV25 captures successive samples of the output of the shaper in sets of three. By fitting the known  $CR-RC$  shaping curve to these samples, the initial time of the hit can be determined to a precision of 2 ns for  $S/N > 25$ , an achievable figure with our sensors if read out individually [13]. For the SVT, six-sample readout and the shortest possible shaping time (35 ns) will be used to best distinguish hits that overlap in time. The APV25 chips are hosted on simple FR4 hybrids since these hybrids and their cooling system are outside the tracking volume. Along with the sensors, these are assembled into large multi-sensor modules, one for each tracking view.

#### 4.3.3. Support Structure

The sensor modules for the SVT consist of a pair of identical half-modules, sandwiched back-to-back around an aluminum cooling block at one end and a similar PEEK spacer block at the other. Figure 7 shows a prototype module assembly. The cooling block provides the primary mechanical support for the module as well as cooling via copper tubes pressed into grooves in the plates. The spacer block defines the spacing between the sensors at the far end of the module, stiffens the module structure, and improves the stability of the sensor alignments.

The total power consumption of the five APV25 chips mounted on the hybrid readout board is about 2 W. Since heating from the leakage current is only significant at a single small spot on the sensor, the dominant

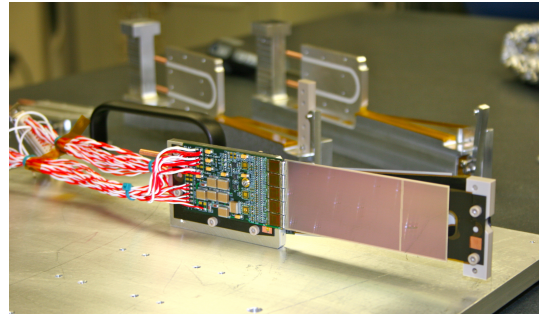


Figure 7: A prototype module assembly (foreground) with the 50 mrad (left) and 100 mrad (right) module assembly fixtures in the background. A pair of cooling blocks and a spacer block can be seen on the fixtures.

heat load on the sensor, event after irradiation, is radiant heat from the inside wall of the vacuum chamber, less than 0.5 W per sensor. The total power consumption budget of about 40 W is removed by a water/glycol mixture circulated through a flexible manifold attached to the copper tubes in the cooling blocks. The total mass flow is about XXXXg/s to operate the sensors at XXXX degrees C.

Each half module consists of a single sensor and a hybrid electronic readout board glued to a polyamide-laminated carbon fiber composite backing. A window is machined in the carbon fiber leaving only a frame around the periphery of the silicon to minimize material. A 50  $\mu\text{m}$  sheet of polyamide is laminated to the surface of the carbon fiber with 1 mm overhang at all openings to ensure good isolation between the backside of the sensor, carrying high-voltage bias, and the carbon fiber which is held near ground. The average support material in the tracking volume is approximately 0.06%  $X_0$  per double-sided module for a total of 0.7% per layer.

#### 4.4. SVT Digitization, Event Building and Data Transmission

The SVT Data Acquisition (DAQ) is a SLAC-standard system using consisting of a single ATCA crate with two Cluster On Board (COB) cards and a 10 Gb/s switch [14]. The COBs connect to Rear Transition Modules (RTM) housing 14-bit ADCs that accept input data from the APV25 chips. The COB house FPGA-based Data Processing Modules (DPM) and the Trigger Interface (TI) to the ECal trigger. This system is capable of 20 kHz operation, whereas upgrades for the full experiment pushes this up to 50 kHz. Power is provided to each hybrid using CAEN power supplies from the decommissioned CDF SVXII detector.

**This needs to be expanded. I should talk about the data reduction and event handling.**

#### 4.5. Production, Assembly and Shipping

Hybrid readout boards and half-modules were assembled at SLAC. Mounting APV25 chips and all wire-bonding and QA testing were performed at University of California, Santa Cruz. Of the sensors tested during production, 90% were capable of 1000 V bias. Hybrids underwent quick QA testing and each half-module was run at low temperature ( $\approx 5^\circ \text{ C}$ ) and fully characterized for pedestals, gains, noise and time response after assembly. All 29 production modules were assembled between mid-February and the end of March, 2012. Module yields were excellent for such a small production. Of 165 APV chips acquired, 150 were used to assemble 30 production hybrids, of which 29 passed QA testing. Of 29 modules built, 28 passed QA testing, leaving 8 spare modules after completion of the SVT. Full-module assembly and mechanical surveys were performed at SLAC in early April 2012 before final assembly, testing and shipping of the SVT to JLab on April 11. A custom shipping container, based on experience at FNAL [15], was built in order to safely send the partly assembled of the SVT. The two fully assembled SVT halves were attached to a baseplate supported by four wire-rope isolators. This plate, covered by a clean lexan cover was mounted inside an inner box surrounded by 4 inches of Polyurethane foam to complete the two-spring construction. At JLab, the entire SVT was integrated with the full DAQ and the power supplies for the first time in the cleanroom, before moving the module-loaded support plates to Hall B for final mechanical assembly and installation inside of the vacuum chamber on April 19.

#### 4.6. Monitoring and Calibration

#### 4.7. Data Analysis and Performance

During the duration of the dedicated photon run all SVT modules and APV25 readout chips were configured to their nominal operating points [16] while all sensors were reverse-bias at 180 V. The sensors were operated within a temperature range of 20 to  $24^\circ \text{C}$  throughout the test run. Multiple calibration runs established a noise level of  $\approx 750 - 850$  electrons which was stable across the SVT modules.

Throughout the duration of the test run, approximately 97% of the 12,780 SVT channels were found to be operating normally. The fraction of dead or noisy channels varied from 2.4% to 4.7%; most of these were due to misconfigured readout chips (2–4 misconfigured

chips out of 100 total) a known noisy half-module, and a couple of known noisy readout chips.

#### 4.7.1. Cluster and Hit Reconstruction

After a trigger is received, six samples of the corresponding output of the APV25 shaper circuit are digitized. The samples from every channel on a sensor surviving the data reduction, described in Sec. ??, are the basis for offline hit reconstruction. The six samples of the APV25 pulse shaper output are fitted to an ideal  $CR - RC$  function to extract the amplitude and the  $t_0$  of the hit. The typical pulse shape obtained is shown in Figure 8 also demonstrates that the SVT was well timed in to the trigger with the rise of the pulse at the 3rd sampling point. These hits are passed through a simple clus-

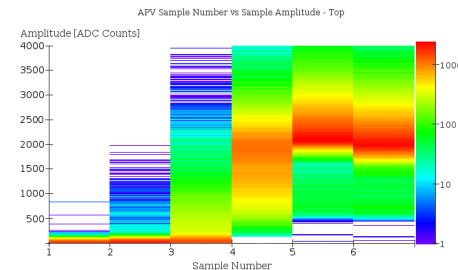


Figure 8: The six pedestal subtracted samples associated with a hit on a track.

tering algorithm which forms clusters by grouping adjacent strips. The position of a cluster on the sensor is determined by a pulse height weighted mean (FIX THIS). With a linear gain up to  $\approx 3$  MIPs, the cluster charge for hits associated with a track follow the characteristic Landau shape as expected, see Fig. 9.

After clustering hits on a sensor, the hit time for each cluster is computed as the amplitude-weighted average of the fitted  $t_0$  channel times. The  $t_0$ -resolution is studied by comparing the cluster hit time with the average of all cluster hit times, the “track time” which has the expected jitter due to clock phase and trigger  $\approx 25$  ns. Figure 10 shows the residual to the individual cluster times. After correcting for offsets from each sensor (time-of-flight, clock phase) the extracted  $t_0$  resolution is 2.6 ns. This is somewhat worse than the  $\approx 2$  ns resolution expected which we attribute to the true pulse shape differing from our idealized fit function which will be improved in the future. Reducing the APV25 pulse shaping time will also improve time resolution. These results show that we can operate with the critical six sample readout mode of the APV25 chip and achieve time

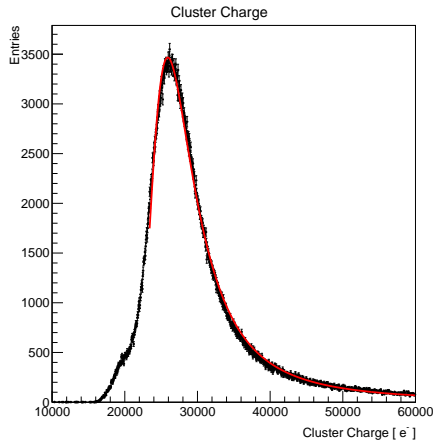


Figure 9: The cluster charge distribution.

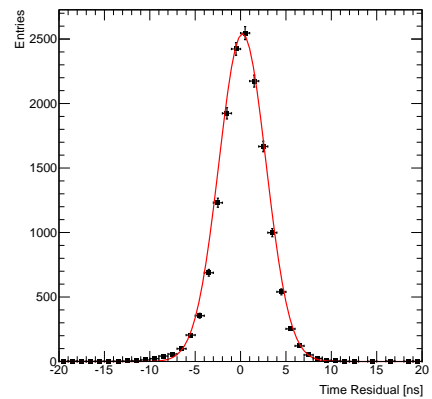


Figure 10: The cluster time residual is for a representative sensor relative to the track time.

resolution adequate for pileup rejection during electron running.

While occupancy was slightly larger than expected, good agreement between data and simulation was found after taking into account dead or noisy channels. The hit efficiency, see Fig 11 was measured to be above 98% and fairly uniform across the SVT.

The spatial resolution of similar microstrip sensors is well established by test beam data, against which the charge deposition model in the simulation is validated. This resolution can be parameterized as a function of the total signal to single-strip noise ( $S/N$ ) and the crossing angle of tracks through the sensor. The single-hit resolution for charged particles with  $S/N > 20$ , as demonstrated here, is relatively constant at approximately 6  $\mu\text{m}$  for tracks that are close to normal to the sensors as in HPS.

#### 4.7.2. Alignment

The SVT was aligned using a combination of optical, laser and touch probe surveys at SLAC and JLab. The optical survey of individual modules with precision of a few microns are combined with a touch-probe survey of the overall SVT support structure, with 25-100 microns precision, to locate the silicon sensor layers with respect to the support plates and the mechanical survey balls on the base plate. After full assembly and installation of the SVT at JLab, a mechanical survey of the SVT base plate position inside the pair spectrometer vacuum chamber is used to determine the global position of the SVT with respect to CEBAF beam line. The resulting survey-based alignment has the position of the silicon sensors correct to within a few hundred microns a more

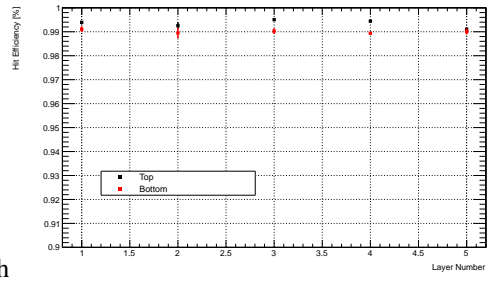


Figure 11: The hit reconstruction efficiency as a function of detector layer.

sophisticated global track-based alignment technique to reach the final alignment precision is used.

#### 4.7.3. Momentum and Vertexing Resolution

By selecting  $e^+e^-$  pairs from the triggered events we are able to study basic distributions of pair production kinematics and in particular those related to our vertex performance. Pairs of opposite charge tracks, one in the top and one in the bottom half of the SVT, with larger than 400 MeV were selected. The pair production kinematics are relatively well reproduced given the alignment of the tracker; Fig. 12 shows the invariant mass and ratio of electron momentum over the sum of electron and positron.

For the vertexing performance the foremost difference compared to electron beam running is that the target was located  $\sim 67$  cm from our nominal target posi-

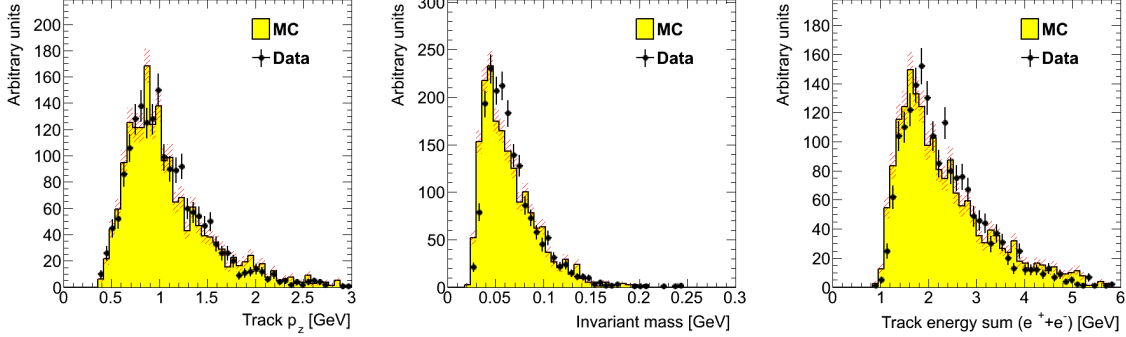


Figure 12: Kinematic distributions for  $e^+e^-$  pairs selected by opposite charged tracks in the top and bottom half of the tracker: track momentum in the top half of the SVT (left), invariant mass (middle) and the sum of the track momentum for the pair.

tion; giving almost collinear tracks in the detector. This degrades the vertex resolution along the beam line compared to that expected in an electron beam with tracks from the nominal target position. Furthermore, tails of the vertex distributions are impossible to study with the finite sample of events from the Test Run. Nevertheless, useful information can still be obtained by studying the vertex distributions. Figure 13 shows the distance of closest approach of the momentum vectors extrapolated in the upstream direction from our analyzing magnet, taking into account the measured fringe field.

While the tails of the vertex distribution expected in electron beam running is not accessible here the fact that the core is relatively well described provides confidence of the description of the amount of material and the multiple scattering description. These are crucial for benchmarking the physics reach of the HPS detector since both the mass and vertex resolution that determine the physics reach are limited by multiple scattering.

## 5. Electromagnetic Calorimeter

The electromagnetic calorimeter just downstream of the tracker uses detectors with comparably short live time and high rate capability. It performs two essential functions for the experiment: triggering and electron identification. The device is highly segmented. It is fast, able to readout at rates comparable to those in the tracker, and able to provide good spatial and energy information to the trigger electronics. Like the tracker system, the electromagnetic calorimeter is split to avoid impinging on the dead zone. The beam and radiative secondaries pass through the calorimeter in vacuum, to avoid generating unnecessary backgrounds.

### 5.1. Purpose and Design Requirements

The electromagnetic calorimeter (ECal) provide the trigger for the data acquisition and will be used for electron identification during the data analysis. The ECal is positioned after the analyzing dipole magnet and cover the full acceptance region of the SVT. It consist of two halves, split in the horizontal beam plane. The gap between upper and lower parts, XXXX mrad (15mrad for electron running), as seen from the target location, is necessary to avoid the "dead zone" where occupancy and radiation prevents any instrumentation to be situated.

The energy of electrons of interest will be in the range  $0.5 - 6.5$  GeV. The ECal modules must have sufficient radiation lengths to absorb the full energy of these scattered electrons, have fine enough granularity to handle a high rate of electromagnetic background and survive large doses of radiation, especially near the beam plane. In addition, it needs to have excellent hit time resolution,  $< 10$  ns, in order to beat down beam backgrounds.

The compact design requirements: high radiation environment , high rate and the presence of high magnetic field, are fulfilled by a lead-tungstate ( $PbWO_4$ ) crystal calorimeter with magnetic field resistant avalanche photodiode (APD) readout. Such crystals has been operational in the inner calorimeter of the CLAS experiment [XXXX] at JLab since 2005 and meet all requirements set by HPS. These crystals were subsequently repurposed for the ECal.

### 5.2. Layout

The modules in the ECal are arranged in two formations, as shown in Fig. 14.

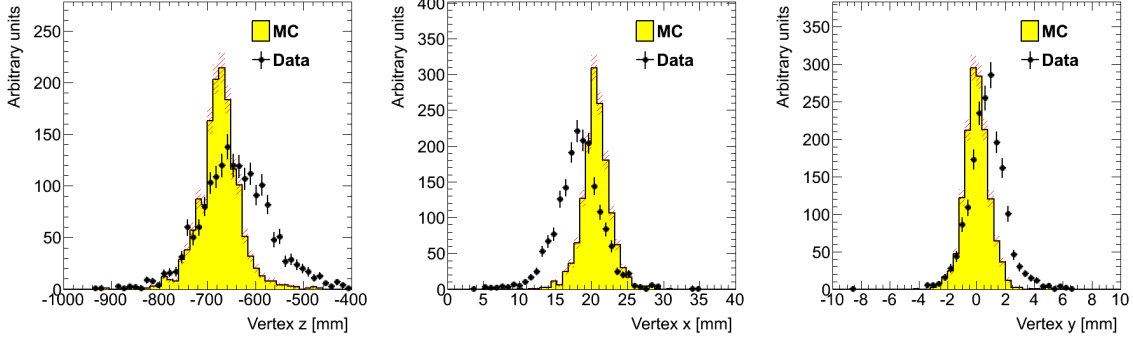


Figure 13: Vertex position represented by the distance of closest approach of the extrapolated momentum vectors upstream of the analyzing magnet. The overall shift from zero in the x-direction is due to a 30 mrad rotation of the SVT with respect to the beam line.

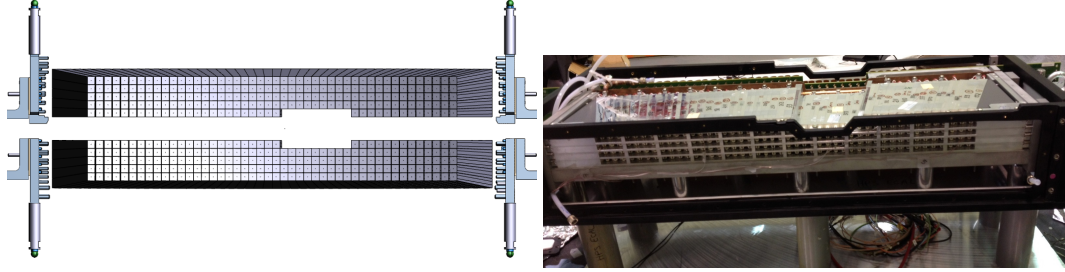


Figure 14: Schematic layout view of the two halves of the ECal (left) and a picture of one half being assembled before installation on beam line (right).

There are 5 layers in each formation. Each layer has 46 crystals except for the layers closest to the beam plane where 9 modules were removed to allow a larger opening for the outgoing electron and photon beams. The ECal is mounted downstream of the analyzing dipole magnet at the distance of about 137 cm from the upstream edge of the magnet. The two ECal modules are positioned just above and below the ECal vacuum chamber, through which the beam, radiated photons, and the wall of flame will pass unimpeded. The innermost edge of the crystals is just 2 cm from the beam.

### 5.3. ECal Components

#### 5.3.1. *PbWO<sub>4</sub>* Crystals

The ECal PbWO<sub>4</sub> crystals, from the same crystals that were used in the IC. The IC calorimeter was assembled from 424 lead tungstate tapered crystals with dimensions of 13.3×13.3 mm<sup>2</sup> (front face), 16×16 mm<sup>2</sup> (rear face) and 160 mm length. The crystals were fabricated with very tight tolerances: 19 μm for 13.3 mm dimension and 13 μm for the 16 mm dimension. Each crystal is wrapped in VM2000 multilayer polymer mirror film.

#### 5.3.2. Support Structure

In order to stabilize the calorimeter's performance, the crystals, APDs, and amplifiers are enclosed within a temperature controlled environment, held constant at the level of 1° F.

#### 5.3.3. Avalanche Photodiode Readout and Preamplifiers

Avalanche Photodiodes (APD) S8664-55 produced by Hamamatsu Corp. are used as photodetectors. They have a 5 × 5 mm<sup>2</sup> active area and quantum efficiency of about 75%. Single APDs were centered on the back ends of the crystals using MeltMount 1.7 thermal plastic adhesive. The low? amplitude signals of APDs are amplified using custom?made preamplifier boards. Figure 15 shows a schematic view of the module assembly.

The gain uniformity of the APDs is on the order of XXXX%; with APD high voltage bias varying by as much as 100V. Since only a limited number of high voltage channels were available during the test, 10 channels were grouped together with an attempt to group modules with similar gains.

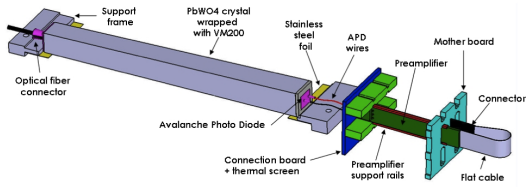


Figure 15: Schematic view of an ECal module.

The signals from the preamplifier boards were sent, through a 2 : 1 signal splitter to a time-to-digital converter and the Flash ADC readout boards discussed in Sec. 6.1.1.

#### 5.4. Calibration and Performance

Of 442 modules, 39 were disabled or disconnected and were not read out by the DAQ. 13 of these were not read out because of a shortage of FADC readout boards (see Sec. 6.1.1). The remainder either had no HV bias on the APD, or were disabled in the FADC software due to noise. In the data, we identified two types of abnormal channels. One FADC was not sending trigger signals correctly, resulting in low efficiency. This affected the 13 channels read out by that FADC. 5 channels were diagnosed as noisy because they had a high incidence of hits out of coincidence with the trigger. A large number of channels were originally misidentified as noisy because they had much higher hit occupancy than neighboring channels. Gain calibration shows that these channels have high gain (and thus lower energy threshold) but are otherwise normal. The abnormal channels were ignored in analysis in order to simplify comparison with Monte Carlo. This leaves 385 useful channels—87% of the ECal.

The noise level of the ECal modules were measured to be approximately 15 MeV. The ECal was operated with an effective readout threshold of 70 MeV.

Modules above thresholds are clustered using a simple robust algorithm described in Sec. 6.2.

##### 5.4.1. Calibration

The noise and pedestal of the readout chain are calibrated by running the ECal readout in a mode where the preamplifier output is sampled every 4 ns in a time window of 100 samples: by looking at a part of the window before the hit, we calibrate the readout channel. The readout threshold

We calibrate gain of the individual ECal channels using the SVT measurement of track momentum and comparison to Monte Carlo simulation. We disable all SVT

and ECal channels in the simulation that were inoperable or noisy in the test run, so any efficiency or bias effects that affect the real data should be reflected in the simulation as well; then we use a formula to compute the “weighted E/p” for a crystal, representing the average E/p for clusters that include the crystal, and iteratively adjust the gains until the weighted E/p is equal for test run data and simulation.

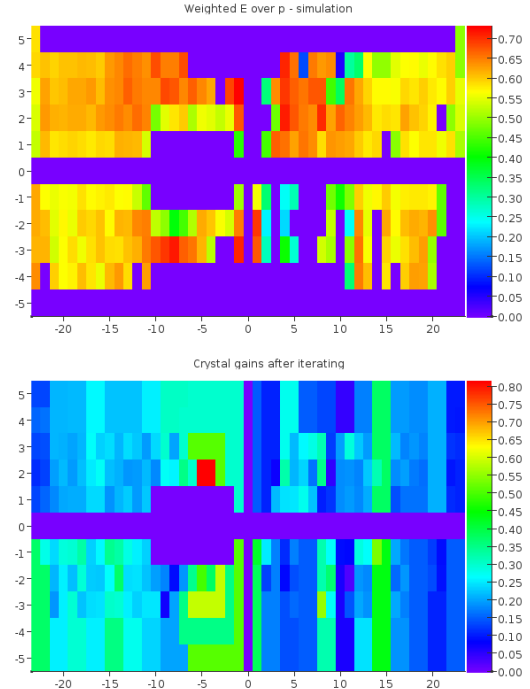


Figure 16: Weighted E/p from Monte Carlo simulation (top), calibrated values of gain in units of MeV per ADC count (bottom).

These gains can then be used to convert from ADC counts in a channel to the energy deposited into that ECal crystal. The other information needed to find the energy of an incident particle is the sampling fraction—the ratio of energy read out from crystals to energy of an incident particle. The conventional sampling fraction, the fraction of incident energy that is deposited in crystals, is approximately 0.9 for the ECal and less at the edges. For our readout, there is additional energy lost because crystals under the readout threshold are not read out. The weighted E/p used in calibration (see Figure 16) is an approximate measurement of sampling fraction, but the sampling fraction is energy-dependent because of the effect of readout threshold. A full computation of sampling fraction can be done using simulation.



Figure 17: A Jefferson Lab FADC250 VXS module.

### 5.5. Monitoring

## 6. Trigger and Data Acquisition

The HPS Test apparatus DAQ handles the acquisition of data for two sub-detectors: the SVT and ECal. It employs two DAQ architectures: the SVT is readout with Advanced Telecom Communications Architecture (ATCA) hardware while the ECal and Muon System use VXS based hardware. The trigger system receives input from the ECal and distributes a trigger signal to all detector sub-systems to read out a selected event.

### 6.1. Electronics

#### 6.1.1. Flash ADC Readout Board

The analog signals from the individual APD's of the ECal (shaped and amplified as described in Sec. ??) are input to a single channel on the 16-channel JLab FADC250 VXS module (FADC), shown in Fig. 17.

Three 20-slot VXS crates are needed to accommodate the system: one for each half of the ECal with 221 channels and one for the Muon System with a total of 232 channels.

The FADCs store 12-bit digitized samples at 250 MHz in 8  $\mu$ s deep pipelines. When a trigger is

received, the appropriate part of the pipeline is accessed. If a FADC signal exceeds a predefined threshold within that time window, the integrated amplitude of a pre-defined number of samples before (NSB) and after (NSA) the signal passed threshold, in addition to the time, are recorded. This scheme significantly compresses the data input to the FADC. During data analysis, a pedestal value is subtracted to obtain the actual summed energy. The main characteristics of the FADC are:

- 12-bit digitizer with sampling rate of 250 Msps,
- $50\Omega$  termination input,
- front-end input range: -0.5V, -1V or -2V (sufficient to avoid signal clipping for large pulse heights),
- nominal charge resolution between 10-39 fC per ADC (see Tab. 3).

Input range (V)	Nominal charge resolution (fC per ADC count)
-0.5	9.76
-1.0	19.53
-2.0	39.06

Table 3: Nominal FADC charge resolution for different front-end input ranges.

As shown in Fig. 18, the FADC has two parallel data paths: the readout and trigger paths. The trigger path runs continuously to report hits to the trigger system. The readout path only reports hits to the DAQ when the FADC receives a trigger.

For the readout path, every FADC has the following parameters:

- the number of samples integrated before the signal crossed threshold ( $NSB$ ),
- the number of samples integrated after the signal crossed threshold ( $NSA$ ),
- the readout threshold, measured in ADC counts.

The number of samples for a given channel integration is the sum of  $NSB + NSA$  samples. It is a fixed gate width pulse integration with no pedestal subtraction where the sum is stored in a 17-bit register for readout (pedestal subtraction happens offline).

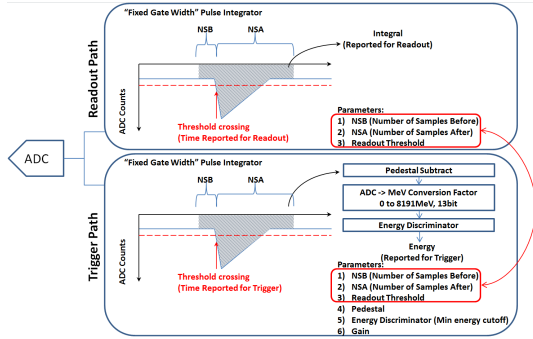


Figure 18: FADC data paths

For the trigger path, every channel has, in addition to  $NS\ B$  and  $NS\ A$ :

- trigger threshold, measured in ADC counts,
- a pedestal,
- a conversion factor (gain) that converts the ADC counts to energy in MeV (with 13 bits: from 0 to 8191 MeV),
- an energy discriminator threshold (minimum energy cutoff).

Note that the threshold for the trigger path can be set independently from the readout threshold. The pedestal value is subtracted from the integrated sum over  $NS\ B + NS\ A$  samples and converted to MeV units using a supplied gain conversion factor. The energy discriminator can be used to cut off low energy pulses before reporting to the Crate Trigger Processor. The values reported to the Crate Trigger Processor are the 13-bit pulse energy and the time at which the pulse crossed the threshold. Data for every channel is sent every 32 ns (if there is no hit a 0 energy pulse is sent) which sets a worst case double pulse resolution of 32 ns for individual channels, but less if pulses occur in adjacent 32 ns windows.

### 6.1.2. Trigger Boards

Describe CTP and SSP?

## 6.2. Trigger

The trigger system is designed to efficiently select  $e^+e^-$ -events by using information from the ECal. The trigger looks for time coincidences of clusters in the top and bottom half of the ECal. The trigger system can be broken down into three sections (see Fig. 19):



Figure 19: Block diagram of the ECAL trigger system consisting of the FADC that samples and digitizes the detector channel signals and sends them for cluster finding in the CTP. The CTP clusters are sent to the SSP where the final trigger decision is taken based on pairs of clusters in both halves of the ECal. The decision is sent to the Trigger Supervisor (TS) that generates the necessary signals to readout the sub-detectors.

- FADC (pulse finding): samples and digitizes the signal pulses from each detector channel. Sends the measured pulse energy and arrival time to the CTP.
- CTP (cluster finding): groups FADC pulses from each half of the ECal into clusters. The cluster energy, arrival time, and hit pattern are sent to the SSP.
- SSP (cluster pair finding): searches for time coincidence of pairs of clusters from the top and bottom half of the ECal and applies topological selections.

The time coincidence window of pairs of clusters in the top and bottom half of the ECal are programmable with 4 ns resolution.

As described above in Sec. 6.1.1, the first stage of the trigger logic is incorporated into the FPGA's on the FADC boards which sends crystal energy and time information to the CTP. With the available 3-bit time information, the CTP looks for time coincidence of crystal signals with 8 ns resolution (limit is 4 ns). The cluster finding algorithm is very fast and makes use of the parallel processing nature of FPGA's by simultaneously searching for 125 clusters, up to 3x3 in size, across the calorimeter crystal array and performs the following tasks:

- Adds energy from hits together for every 3x3 square of channels in ECal.
- Hits are added together if they occur (leading edge) within a programmable number of 4 ns clock cycles of each other (HPS will use 8 ns time coincidence time interval).
- If the 3x3 energy sum is larger than the programmable cluster energy threshold and the sum is greater than any neighboring 3x3 windows, the CTP reports the cluster parameters to the SSP.

The CTP evaluates all hits in its half of the calorimeter every 4 ns. A programmable time window is used to allow hits that are out of time with each other to be considered as part of a cluster sum. This is done by reporting hits when they occur and then reporting them again for the next  $N$  number of 4 ns clock cycles, where  $N \in [0, 7]$ . This is useful to deal with skew and jitter that develop from the detector, cabling, and electronics. As described above, the CTP only selects the 3x3 window with the highest energy sum of its neighbors. This filtering is applied to deal with overlapping clusters and cases where the cluster is larger than a 3x3 window.

The final trigger decision is made in the CTP and Sub-System Processor (SSP). The Trigger Supervisor generates all necessary signals and controls the entire DAQ system readout through the Trigger Interface (TI) units. The TI units are installed in every crate that participate in the readout process.

The trigger system is free-running and driven by the 250 MHz global clock and has essentially zero dead time at occupancies expected by HPS. The Trigger Supervisor can apply dead time if necessary, for example on a ‘busy’ or ‘full’ condition from front-end electronics. The system is designed to handle trigger rates above 50 kHz and a latency set to  $\approx 3 \mu\text{s}$  to match that required by the SVT APV25 chip.

### 6.2.1. Performance

As discussed above, the trigger and DAQ integrate pulses differently to measure hit energy. The trigger integrates using a time-over-threshold window, and the DAQ readout integrates using a constant window (5 samples before and 30 samples after a threshold crossing). For every event, the trigger reports the trigger decision as a bit mask (top trigger, bottom trigger, or both) and the time the trigger fires.

We study trigger performance by simulating the trigger for each event and comparing to how events were actually triggered. First, we simulate the FADC readout board to convert from readout hits (constant integration window) to trigger hits (time-over-threshold integration). We then simulate the CTP clustering algorithm and the trigger decision before we compare the trigger decision and trigger time reported by the simulation to what was reported by the real trigger.

To eliminate trigger bias in checking the trigger decision, we use a tag and probe method. To check trigger performance in one half of the ECal, we tag events where there was a trigger in the other half, and exactly one probe cluster in the ECal half under test. We then measure trigger efficiency (proportion of tagged events where there was a trigger) as a function of ADC counts

and energy of the probe cluster. These turn-on curves are shown for the top half of the ECal in Fig. 20.

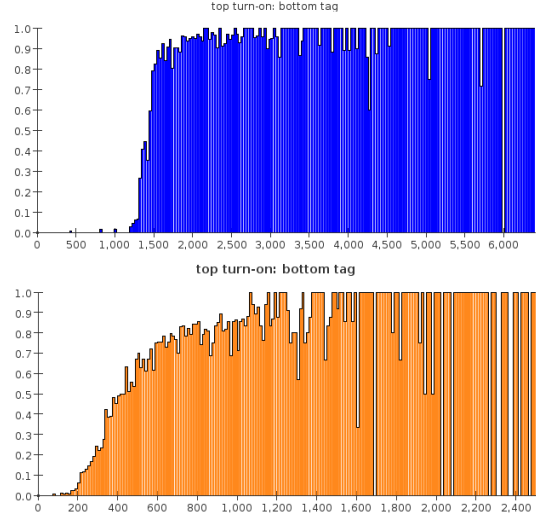


Figure 20: Trigger turn-on as a function of probe cluster ADC counts (top) and probe cluster energy in MeV (bottom). Both plots are for the top half of the ECal; bottom is similar. Energy is not corrected for sampling fraction.

The trigger threshold is seen to be 1280 ADC counts as expected. The threshold is not perfectly sharp in this analysis because of uncertainties in the conversion from readout to trigger hits but based on comparisons with Monte Carlo simulation we believe the trigger worked exactly as specified. The trigger threshold in terms of cluster energy is very uneven for two reasons; gain variations between different ECal crystals lead to threshold variations and the nonlinearity of the time-over-threshold integral means that the effective threshold is higher for clusters that span multiple crystals. Overall the trigger appears to have functioned exactly as intended. Changes planned for the next run (constant integration window and per-crystal gain calibration constants for the trigger) will solve both of the issues that led to threshold variations in the test run.

### 6.3. Data Acquisition and Online Computing

For the ECal, every VXS crate contains a Readout Controller (ROC) that collects digitized information, processes it, and sends it on to the Event Builder (EB). The ROC is a single blade Intel-based CPU module running DAQ software under CentOS Linux OS. For the SVT ATCA system, the ROC application runs on an embedded processor situated on the ATCA main board.

The EB assembles information from the SVT, ECal and Muon System ROCs into a single event which is passed to the Event Recorder (ER) that writes it to a RAID5-based data storage system capable of handling up to 100 MB/s. The EB and other critical components run on multicore Intel-based multi-CPU servers. The DAQ network system is a Foundry router providing high-speed connections between the DAQ components and to the JLab computing facility. The SVT ROC, which must handle large data volumes, has a 10 Gbit/s link to the Foundry router, while a 1 Gbit/s link is adequate for the ECal and Muon System. A 10 Gbit/s uplink to the JLab computing facility is used for long-term storage.

The SVT DAQ is described in more details in Sec. 4.4.

## 7. Multiple Coulomb Scattering Distributions

Occupancies close to the beam create many of the key challenges in the HPS experiment and determine the limits of sensitivity to low  $A'$  masses. These occupancies are dominated by electrons which have multiple Coulomb scattered (MCS) to relatively large angles in the converter. Because HPS is sensitive to scattering angles far out on the tail of the MCS distribution, well beyond the angles important in other experiments, care must be taken to ensure our simulations are correct in this regime.

### 7.1. Multiple Coulomb Scattering Models

In particular, GEANT4 [17] overestimates the MCS rate by a factor of two at large angles. One of the main goals of the HPS Test was to evaluate the description of the tails of the multiple Coulomb scattering in order to gain further confidence in the expected detector occupancy in the full HPS experiment.

Figure 21 gives a schematic view of the main differences between the photon and electron beam setup. In particular, the angular distribution of the pair produced electron and positron emerging from the converter has comparable contributions from *i*) the pair production angle and *ii*) the MCS of the electron and positron in the converter after production. By measuring the scattering rate at several different converter thicknesses we can vary the contribution from MCS to confirm our model of MCS despite the fact that all data was taken with a photon beam.

### 7.2. Running Conditions

Data was taken at three different converter thicknesses with a beam current varying between 30–70 nA,

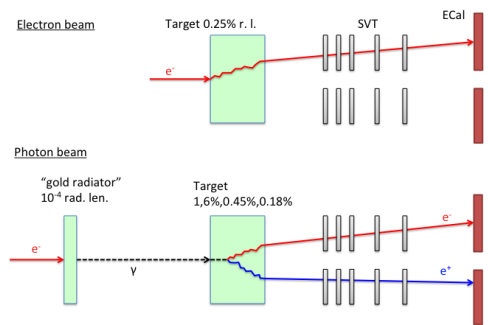


Figure 21: Schematic comparison of HPS Test run photon beam compared to the HPS electron beam.

Converter thickness (%r.l.)	Duration (s)	$e^-$ on converter (nC)
1.6	911	24385.9
0.18	2640	193508.9
0.45	2149	140709.9
0	1279	88079.6

Table 4: Measured integrated currents for the dedicated photon runs.

see Tab. 4. The photon beam line during the test run produced a relatively large fraction of pairs originating upstream of the converter. This contribution was measured during data taking with “empty” converter runs i.e. removing the converter but with all other conditions the same. The upstream background measured in the “empty” converter runs was subtracted from the other runs, properly normalized using the measured integrated currents.

### 7.3. Measured Angular Distributions

For this analysis, we measure angular distribution of electrons and positrons using the ECal. Cluster reconstruction was done using the algorithm described in Sec. ???: build clusters around seed hits (hits above a “seed” energy threshold and with greater energy than any neighboring hits), and add all neighboring hits above an “add” energy threshold. Hit energy is calibrated by matching track momentum to cluster energy, as described in Sec. 5.4.1.

The measured angular distribution in the ECal for the three converter thicknesses are shown in Fig. 22 (left).

The background fraction for the three converter thicknesses was 16%, 52% and 71% for converter thick-

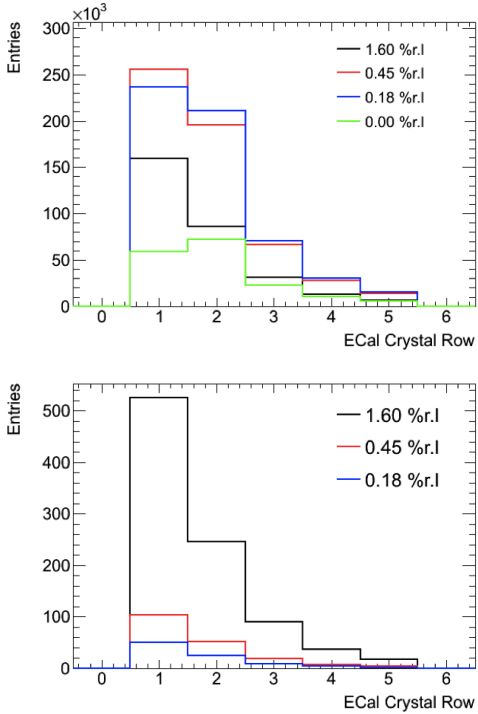


Figure 22: Measured raw vertical angular distributions before (top) and after (bottom) normalization and background subtraction.

nesses of 1.6%, 0.45% and 0.18%, respectively. The background fraction was also cross-checked by pointing back tracks reconstructed in the SVT to identify the fraction of tracks not emanating from the converter. We also checked that the contribution from photons to our triggered sample was less than 2% (without angular selections which would further reduce the contribution).

These measured angular distributions are compared to simulation to validate the modeling of the MCS. As described in more detail in Appendix XXXX, EGS5 [18] is used to generate the electromagnetic interactions in the converter while GEANT4 is used to simulate the particles after the converter. Figure 23 shows the angular distribution comparing data and EGS5 normalized to 1 s of beam at 90 nA beam current.

The total rate measurements are in Fig. 24 and summarized in Tab. 5.

The total systematic uncertainty was estimated to be between 10-18% depending on the run including: a 5% uncertainty on the integrated current normalization,

Converter (% r.l.)	1.60	0.45	0.18
EGS5	$1162 \pm 112$	$255 \pm 28$	$94 \pm 17$
GEANT4	$2633 \pm 250$	$371 \pm 38$	$114 \pm 18$
Observed	$1064 \pm 2$	$196 \pm 1$	$92 \pm 1$

Table 5: Observed and predicted number of events for 1 s of beam at 90 nA for three different converter thicknesses. The uncertainty on the prediction includes systematic uncertainties.

alignment of the ECal, uncertainty from the background normalization, and limited Monte Carlo statistics.

#### 7.4. Conclusion

In summary, the accurate modeling of the MCS is fundamental to estimate occupancies and trigger rates for HPS. EGS5 predicts the correct angular distribution across all converter thicknesses while GEANT4 overestimates the rates; with the disagreement increasing with larger converter thickness. This preliminary result verifies our modeling of the MCS using EGS5 for HPS.

## 8. Summary and Outlook

This paper reviewed the HPS Test Run apparatus, a simplified version of that planned for the full HPS experiment, and demonstrates the feasibility of the detector technologies proposed for silicon tracker, ECal, and data acquisition systems. It documents the performance of the trigger, data acquisition, silicon tracker, and ECal and shows that the performance assumed in calculating the physics reach of the experiment is realistic. Of particular importance, data from dedicated photon beam running has been used to compare the observed trigger rates with that expected in simulation. The trigger rate is almost entirely due to photons which have converted to  $e^+e^-$  upstream of HPS and is sensitive to the multiple Coulomb scattering of electrons and positrons in the conversion target. Since scattered primary beam is the dominant source of occupancy in running HPS in an electron beam, good agreement between data and simulation confirm the background simulation used to benchmark the physics reach of the HPS experiment.

In addition to this important test of our background simulation, the test run accomplished the following goals:

1. More than 97% of SVT channels functioned properly
2. SVT readout signal to noise of 25.5, required to achieve the expected spatial and temporal resolutions

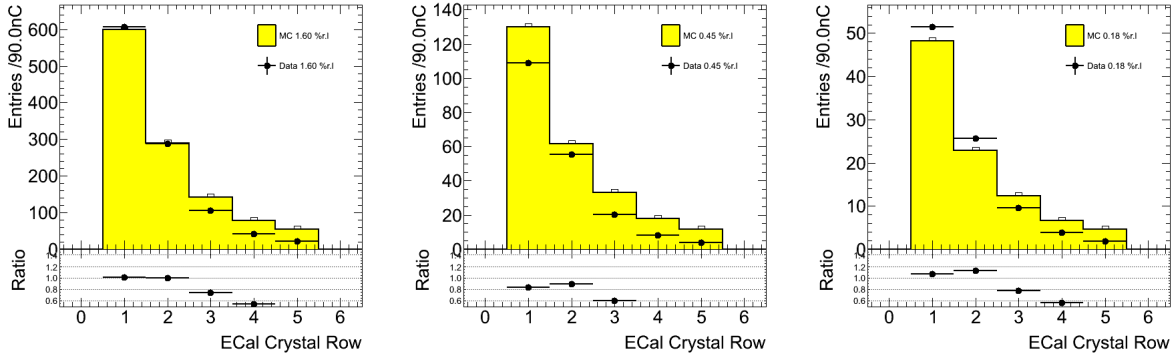


Figure 23: Comparison between the observed and predicted angular distribution using EGS5 for a converter thickness of 1.6% (left), 0.45% (middle) and 0.18% (right). Only statistical uncertainties are included.

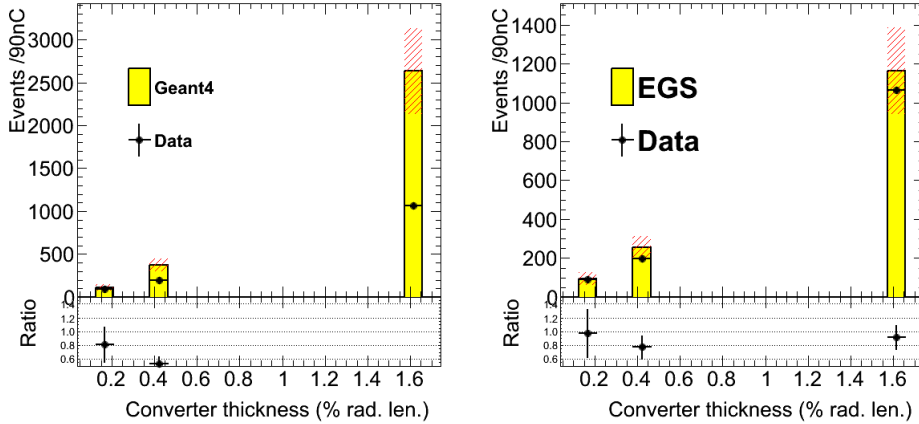


Figure 24: The measured rate as a function of converter thickness comparing GEANT4 (left) and EGS5 (right).

3. SVT hit time resolution of 2.6 ns, proving hit time reconstruction will work for HPS
4. SVT hit efficiency greater than 98%
5. Survey-based SVT alignment performed as expected and will allow track-based alignment
6. 87% of ECal crystals functioned properly, with defects to be corrected by planned ECal upgrades
7. The ECal has been calibrated using SVT tracks
8. The SVT and JLab DAQ were successfully integrated
9. The trigger functioned as designed; FADC trigger rate was tested to greater than 100 kHz

While the Test Run successfully allowed us to test many aspects of the HPS experiment, there were limitations to what could be achieved in some key areas such as mass resolution and vertexing performance. In particular, the low statistics and lack of resonances or scattered beam electrons prohibits a direct analysis of the

momentum and tails of the vertex distribution. However, for both of these performance parameters, the observed agreement between data and simulation in key distributions supports the performance expected for the proposed experiment.

### 8.1. Lessons Learned

In the process of developing the HPS Test design, it was found that this simple system was capable of delivering a surprising fraction of the physics potential anticipated for the full experiment. With this in mind, we have proposed a new design for the HPS detector that builds upon the HPS Test, principally by addressing the compromises made for HPS Test to ensure the best possible performance for A' physics within the envelope of the existing beam line layout and analyzing magnet. For the SVT, this design uses the same sensors, readout chips, and module concept and for the ECal the crys-

tal and detector layout will be identical, retaining the most successful elements of the test run apparatus and addressing the weaknesses identified during assembly and operation to ensure the success of the experiment. The new SVT layout restores the sixth layer for more robust tracking, adds acceptance in the deeper layers to increase sensitivity and provides better silicon cooling to improve longevity. Other major updates needed for the full experiment are updates to the SVT electronics and DAQ; improving connectivity and cabling, moving digitization closer to the front-end electronics and updating the data reduction, event handling and trigger synchronization to reach 50kHz trigger rates. This first generation of the full experiment will be ready to take physics data when CEBAF begins operation again in 2014.

## References

- [1] O. Adriani, et al. (PAMELA Collaboration), An anomalous positron abundance in cosmic rays with energies 1.5-100 GeV, *Nature* 458 (2009) 607–609.
- [2] M. Ackermann, et al. (Fermi LAT Collaboration), Measurement of separate cosmic-ray electron and positron spectra with the Fermi Large Area Telescope, *Phys.Rev.Lett.* 108 (2012) 011103.
- [3] B. Holdom, Two U(1)'s and Epsilon Charge Shifts, *Phys.Lett.* B166 (1986) 196.
- [4] N. Arkani-Hamed, D. P. Finkbeiner, T. R. Slatyer, N. Weiner, A Theory of Dark Matter, *Phys.Rev.* D79 (2009) 015014.
- [5] D. Tucker-Smith, N. Weiner, Inelastic dark matter, *Phys.Rev.* D64 (2001) 043502.
- [6] O. Adriani, et al. (PAMELA Collaboration), PAMELA results on the cosmic-ray antiproton flux from 60 MeV to 180 GeV in kinetic energy, *Phys.Rev.Lett.* 105 (2010) 121101.
- [7] J. D. Bjorken, R. Essig, P. Schuster, N. Toro, New Fixed-Target Experiments to Search for Dark Gauge Forces, *Phys.Rev.* D80 (2009) 075018.
- [8] A. G. et al. (HPS Collaboration), HPS Heavy Photon Search Proposal, 2010.
- [9] I. Rashevskaya, S. Bettarini, G. Rizzo, L. Bosisio, S. Dittongo, et al., Radiation damage of silicon structures with electrons of 900-MeV, *Nucl.Instrum.Meth.* A485 (2002) 126–132.
- [10] N. A. Graf, org.lcsim: Event reconstruction in Java, *J.Phys.Conf.Ser.* 331 (2011) 032012.
- [11] D. S. Denisov, S. Soldner-Rembold, D0 Run IIB Silicon Detector Upgrade: Technical Design Report (2001).
- [12] M. French, L. Jones, Q. Morrissey, A. Neviani, R. Turchetta, et al., Design and results from the APV25, a deep sub-micron CMOS front-end chip for the CMS tracker, *Nucl.Instrum.Meth.* A466 (2001) 359–365.
- [13] M. Friedl, C. Irmler, M. Pernicka, Readout of silicon strip detectors with position and timing information, *Nucl.Instrum.Meth.* A598 (2009) 82–83.
- [14] R. Larsen, Emerging New Electronics Standards for Physics, *Conf.Proc.* C110904 (2011) 1981–1985.
- [15] J. Howell, B. Cooper, IHEP Telescope Shipping Container, 2010.
- [16] L. Jones, APV25-S1: User guide version 2.2, RAL Microelectronics Design Group, 2011.
- [17] S. A. et al., Geant4a simulation toolkit, *Nucl.Instrum.Meth.* A506 (2003) 250 – 303.
- [18] H. Hirayama, Y. Namito, A. Bielajew, S. Wilderman, W. Nelson, The EGS5 Code System, 2005.